Stellar and thermal neutron capture cross section of ⁹Be

A. Wallner, ^{1,2,*} M. Bichler, ³ L. Coquard, ⁴ I. Dillmann, ^{4,†} O. Forstner, ^{2,‡} R. Golser, ² M. Heil, ^{4,§} F. Käppeler, ⁴ W. Kutschera, ² C. Lederer-Woods, ⁵ M. Martschini, ² A. Mengoni, ⁶ S. Merchel, ⁷ L. Michlmayr, ² A. Priller, ² P. Steier, ² and M. Wiescher⁸

¹Department of Nuclear Physics, Research School of Physics and Engineering,

The Australian National University, Canberra, ACT 2601, Australia

²VERA Laboratory, Faculty of Physics, University of Vienna, Austria

³Atominstitut, Vienna University of Technology, Austria

⁴Karlsruhe Institute of Technology (KIT), Campus North, Institute of Nuclear Physics, PO Box 3640, Karlsruhe, Germany

⁵School of Physics and Astronomy, University of Edinburgh, United Kingdom

⁶CERN, CH-1211 Geneva 23, Switzerland

⁷Helmholtz-Zentrum Dresden-Rossendorf, Helmholtz Institute Freiberg for Resource Technology, 01328 Dresden, Germany ⁸Department of Physics and Joint Institute of Nuclear Astrophysics, University of Notre Dame, Notre Dame, Indiana, USA



(Received 21 August 2018; revised manuscript received 22 October 2018; published 14 January 2019; corrected 30 May 2019)

The neutron capture cross section of $^9\mathrm{Be}$ for stellar energies was measured via the activation technique using the Karlsruhe Van de Graaff accelerator in combination with accelerator mass spectrometry at the Vienna Environmental Research Accelerator. To characterize the energy region of interest for astrophysical applications, activations were performed in a quasistellar neutron spectrum of kT=25 keV and for a spectrum at $E_n=473\pm53$ keV. Despite the very small cross section, the method used provided the required sensitivity for obtaining fairly accurate results of 10.4 ± 0.6 and $8.4\pm1.0~\mu\mathrm{b}$, respectively. With these data it was possible to constrain the cross section shape up to the first resonances at 622 and 812 keV, thus allowing for the determination of Maxwellian-averaged cross sections at thermal energies between kT=5 and 100 keV. In addition, we report a new experimental cross section value at thermal energy of $\sigma_{\mathrm{th}}=8.31\pm0.52$ mb.

DOI: 10.1103/PhysRevC.99.015804

I. INTRODUCTION

In the seminal papers by Burbidge *et al.* [1] and Cameron [2] the origin of the elements heavier than iron has been ascribed in about equal parts to the slow (*s*) and rapid (*r*) neutron capture processes. Meanwhile, the mechanisms of the *s* process could be identified as being linked to the red giant phase of stellar evolution. The so-called main and weak *s*-process components are occurring in thermally pulsing low-mass asymptotic giant branch (AGB) stars [3–5] and in massive stars [6–8], respectively. Based on extensive observations and on the knowledge of the related neutron physics data [9] the *s*-process abundances are fairly well determined.

Published by the American Physical Society under the terms of the Creative Commons Attribution 4.0 International license. Further distribution of this work must maintain attribution to the author(s) and the published article's title, journal citation, and DOI.

On the contrary, the situation for the short time-scale r process remains rather unclear. In general, core collapse supernovae or neutron star mergers are considered as potential sites because both scenarios can provide the required extremely high neutron densities. Recent observations are compatible with neutron-star mergers as the cosmic origin of the r-process elements [10,11], another promising scenario for explosive nucleosynthesis are neutrino-driven winds in core-collapse supernovae [12,13]. However, quantitative models are yet missing [14], partly because of the persisting difficulties with the associated hydrodynamics in supernova explosions [15,16] and partly because of the complex nuclear reaction network that comprises several thousands of reactions on short-lived neutron-rich nuclei that have no experimental information yet [17]. The high temperatures and densities in neutrino-driven winds in core-collapse supernovae close to the nascent neutron star leads to nuclear statistical equilibrium between α particles and nucleons. As the temperature drops, ¹²C and ⁹Be can be formed in three-particle fusion processes bridging the instability gaps at A = 5 and A = 8 [18,19]. In the following α process, heavier nuclei are formed by a sequence of α captures combined with (n, γ) and (p, γ) reactions depending on the neutron density in the wind.

In this context the role of the ${}^{9}\text{Be}(n, \gamma){}^{10}\text{Be}$ reaction is an open issue because only theoretical predictions exist so far due to the complete lack of experimental data. The considerable uncertainties of these predictions in the astrophysically

^{*}anton.wallner@anu.edu.au

[†]Present address: TRIUMF, Vancouver BC, Canada.

[‡]Present address: Friedrich-Schiller-Universität Jena and Helmholtz-Institut Jena, 07743 Jena, Germany and GSI Helmholtzzentrum für Schwerionenforschung, 64291 Darmstadt, Germany.

[§]Present address: GSI Helmholtzzentrum für Schwerionenforschung GmbH, Darmstadt, Germany.

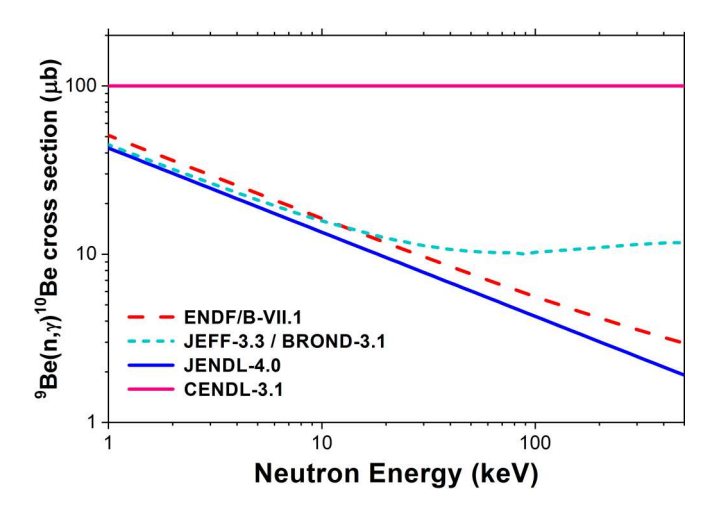


FIG. 1. The evaluated (n, γ) cross section of ⁹Be from the main data libraries ENDF/B-VII.1 [20], JEFF-3.3 [22], JENDL-4.0 [21], BROND-3.1 [23], and CENDL 3.1 [24].

relevant energy range between 1 and 500 keV are reflected by the discrepancies among the evaluated (n, γ) cross sections of 9 Be from the main data libraries shown in Fig. 1.

While only an energy dependence following a E_n^{-a} law was adopted in ENDF/B-VII.1 [20] and JENDL-4.0 [21], a more complex structure was considered for the JEFF-3.3 data [22] (and followed partly by Ref. [23]), which takes potential resonance contributions and the p-wave part of the direct radiative capture (DRC) component into account. In contrast a pure constant cross-section value of $100 \,\mu b$ is assumed in CENDL-3.1 [24].

The more complex structure in the cross section is also supported by unpublished experimental data for the ${}^9\mathrm{Be}(n,\gamma){}^{10}\mathrm{Be}$ cross section in the keV range, which were obtained in a time-of-flight experiment at the Tokyo Institute of Technolgy (TIT) [25] utilizing the online detection of the prompt capture γ -rays (see also Sec. IV). The work reported here aims at resolving these discrepancies by cross-section measurements at 25 keV and near 500 keV neutron energy.

In addition, the thermal capture cross section was measured with the same approach, independent of previous methods. The compilation of Mughabghab [26] and Pritychenko and Mughabghab [27] lists a thermal cross section of $\sigma_{th}=8.49\pm0.34$ mb. A recent highly precise value of $\sigma_{th}=8.27\pm0.13$ mb was published by Firestone and Révay [28] based on a complete knowledge of the neutron capture γ -ray decay schemes. Our method applied in this work is completely independent of the decay scheme of $^{10}\text{Be},$ as AMS directly counts the number of produced atoms rather than measuring de-excitation of excited states.

The experimental method is described in Sec. II followed by the data analysis and the obtained results in Sec. III. Based on the measured data, Maxwellian-averaged cross sections are presented in Sec. IV.

II. MEASUREMENTS

In the astrophysically relevant energy range, ⁹Be belongs to the handful of isotopes among the entire periodic table

(together with carbon, nitrogen, oxygen, and 2 H), which are unique for their extremely small (n, γ) cross sections of only a few μ b. Accordingly, very sensitive techniques are required for a successful measurement. In particular, as the reaction product 10 Be has a long half-life ($(t_{1/2} = 1.387 \pm 0.012 \text{ Myr})$ [29,30], decay counting is no option due to the low production rates and consequently the low decay rates.

Activation by high-intensity neutron irradiations combined with accelerator mass spectrometry (AMS) [31–34] offers an extremely powerful tool to measure cross sections through ultra-low isotope-ratio detection, irrespective of half-lives, and decay schemes of the reaction products. The analysis of activated samples via the AMS method was successfully introduced for the study of the neutron-capture cross section of ⁶²Ni [35] and extended to a number of other neutron induced reactions [33,36–42].

The combination of activation and AMS represents an independent and complementary approach to time-of-flight (TOF) measurements [42]. Activation measurements provide the additional advantage that the continuous direct radiative capture (DRC) contributions, which are usually not distinguishable from backgrounds in TOF measurements, are included automatically.

A. Activations

The present measurements of the ${}^{9}\text{Be}(n,\gamma){}^{10}\text{Be}$ cross sections at keV energies were carried out by neutron irradiations at the Karlsruhe Van de Graaff accelerator as described in Ref. [43] and subsequent AMS analyses of the activated samples at the Vienna Environmental Research Accelerator (VERA) [33,34,44–46]. Thermal neutrons were produced at the TRIGA Mark-II reactor at the Atominstitut in Vienna (ATI).

The long-lived radionuclide 10 Be is one of the routinely measured radionuclides in AMS with typical isotope ratios of 10 Be/ 9 Be = 10^{-11} to 10^{-13} at/at in most applications. According to the available neutron flux and in view of the extremely small (n, γ) cross section of 9 Be, the irradiations at the Karlsruhe Van de Graaff accelerator were expected to yield 10 Be/ 9 Be isotope ratios of only $\sim 10^{-14}$ at/at.

As Be-containing materials are a priori not free of natural ¹⁰Be, a series of test runs were required to identify a potential sample material with low intrinsic (natural) ¹⁰Be content but also for optimizing the VERA setup for this work and to quantify the machine background at VERA in AMS measurements of ¹⁰Be [33,47].

1. Samples

The samples for activations were prepared from selected batches that had been carefully characterized with AMS at VERA. Commercial BeO powder (Alfa Aesar) with an intrinsic $^{10}\text{Be/}^9\text{Be}$ ratio of $(1.38\pm0.06)\times10^{-14}$ at/at was used for the samples BeO-1 and BeO-2 at KIT (see Table I). Eventually, BeO powder, extracted from Phenakite (Be₂SiO₄) [48], was found in the course of this project with a significantly lower ratio of $(0.41\pm0.13)\times10^{-14}$ at/at and was used for sample BeO-3.

TABLE I. Samples prepared for keV-neutron irradiations at KIT.

Sample ^a	Mass (mg)	Thickness (mm)	intrinsic ¹⁰ Be content ^b ¹⁰ Be/ ⁹ Be (10 ⁻¹⁴ at/at)	Irradiation time (d)
BeO-1	63.0	1.3	1.38 ± 0.06	15.4
BeO-2	67.1	1.4	1.38 ± 0.06	10.4
BeO-3	19.4	0.4	0.41 ± 0.13	4.12

^aAll samples 6 mm in diameter.

The samples were thin pellets 6 mm in diameter pressed from BeO powder. During the irradiations they were sandwiched between thin gold foils of the same diameter, which served as neutron flux monitors. In the 25 keV quasi-Maxwell-Boltzmann spectrum these foils were $30-50\,\mu\mathrm{m}$ in thickness, but due to the higher flux $20-\mu\mathrm{m}$ -thick gold foils have been used for the second irradiation at a mean neutron energy of 473 keV.

For the thermal activations an amount of about 1100 mg BeO powder (Alfa Aesar, the same material as used for BeO-1 and BeO-2 at KIT)), was encapsulated in plastic vials (see Table II). These samples had the same intrinsic 10 Be/ 9 Be ratio of $(1.38 \pm 0.06) \times 10^{-14}$.

2. keV neutron production and irradiations at KIT

The irradiations were carried out at the Karlsruhe Van de Graaff accelerator using the $^7\text{Li}(p,n)^7\text{Be}$ reaction for neutron production. Metallic Li layers of 30- μ m thickness, evaporated onto a water-cooled Cu backing, 1 mm in thickness, served as targets for average beam currents of 80 to 90 μ A, which could be maintained during the long-term irradiations of several days.

Activations were performed at two proton energies: a quasistellar neutron spectrum was produced at $E_p = 1912 \text{ keV}$, 31 keV above the threshold of the $^7\text{Li}(p,n)^7\text{Be}$ reaction at 1881 keV. Due to reaction kinematics, all neutrons are emitted into a forward cone of 120° opening angle. The spectrum integrated over that neutron field allows one in very good approximation to determine directly the cross section averaged over a Maxwell-Boltzmann distribution for a thermal energy of kT = 25 keV (quasi-Maxwell-Boltzmann spectrum) [43]. The samples were placed in contact with the neutron production target at the position of the highest flux. A schematic sketch of the setup used for the irradiation is shown in Fig. 2.

A second proton energy of $E_p = 2284$ keV was chosen to produce a neutron spectrum with 473 ± 53 keV FWHM

TABLE II. Samples prepared for neutron irradiations at ATI (thermal).

Sample ^a	Mass (mg)	Intrinsic ¹⁰ Be content ^b ¹⁰ Be/ ⁹ Be (10 ⁻¹⁴ at/at)	Irradiation time (s)
BeO-ATI1	1123	1.38 ± 0.06 1.38 ± 0.06	550
BeO-ATI2	1180		3595

^aBeO powder filled into Eppendorf vials.

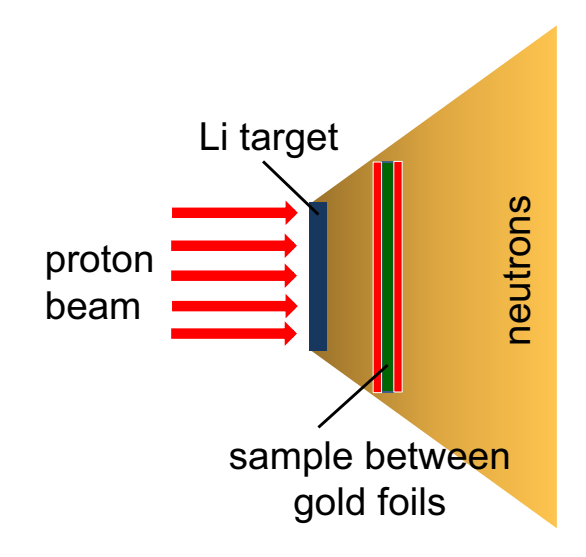


FIG. 2. Schematic setup used for the neutron activations at the Karlsuhe Van de Graaff accelerator.

for constraining the contributions from DRC and from the resonances at 622.0 and 811.8 keV [26]. Due to the higher proton energy, neutron emission is nearly isotropic in this case. Therefore, a distance of 3 mm was chosen between the

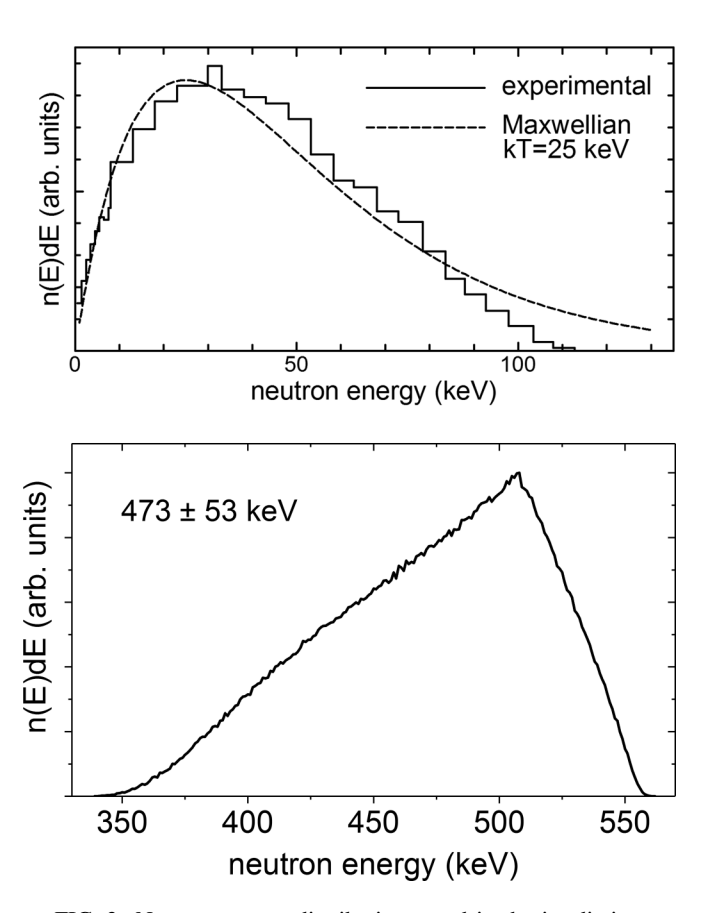


FIG. 3. Neutron energy distributions used in the irradiations at KIT. The upper panel results for protons impinging on a Li target with an energy of 1912 keV and the lower panel for protons with an energy of 2284 keV, respectively.

^bBefore irradiation.

^bBefore irradiation.

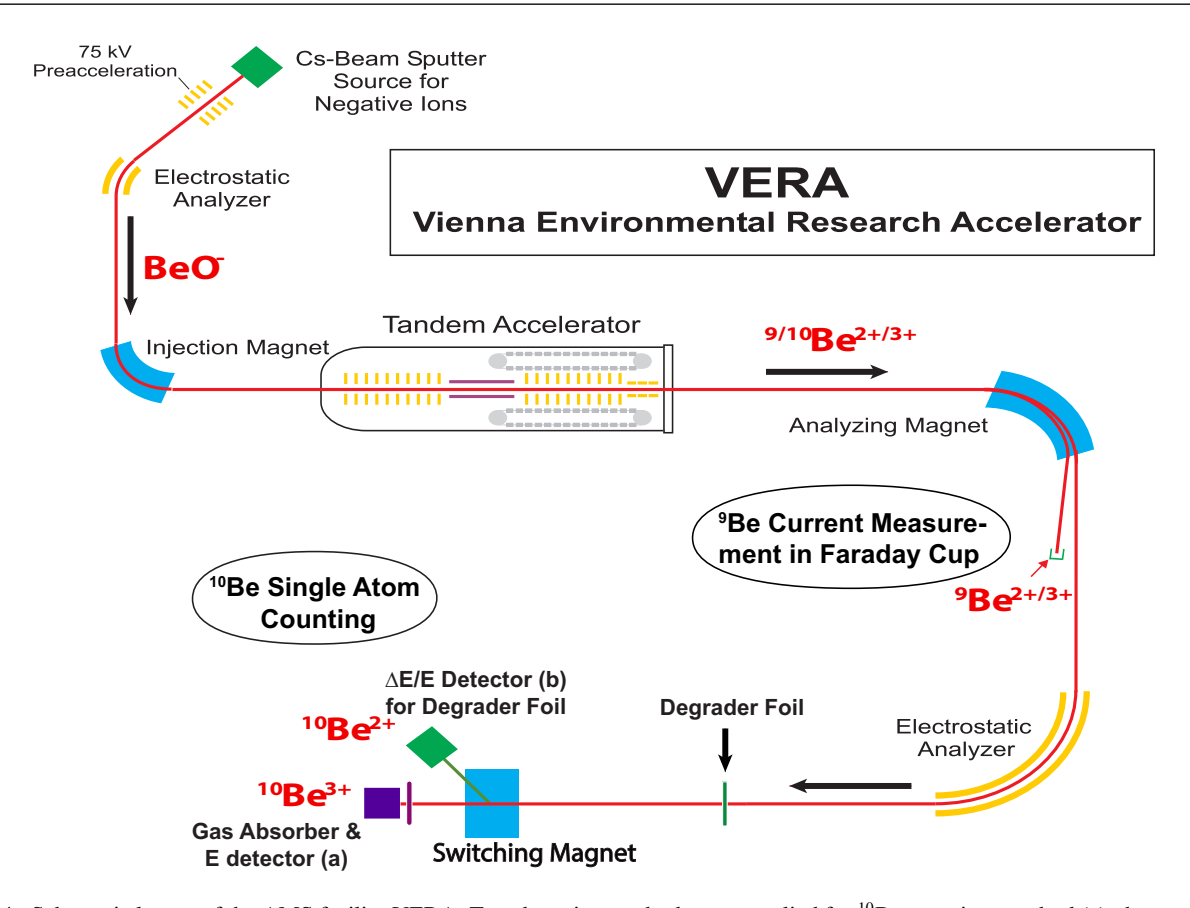


FIG. 4. Schematic layout of the AMS facility VERA: Two detection methods were applied for 10 Be counting: method (a), the gas absorber method, with 10 Be $^{3+}$ passing the switching magnet undeflected and with 10 B stopped in fromt of the E detector, and method (b), the Δ E/E detector setup which is used in combination with a thick degrader foil and the 40 degree exit of the switching magnet for separating the isobar 10 B from the rare nuclide 10 Be $^{2+}$ (see text for details).

actual Li layer and the center of the samples for reducing the background due to neutron scattering in the target and for restricting the energy range of the neutron flux at the position of the sample.

The resulting neutron spectrum was calculated with the actual irradiation parameters as input for the interactive code PINO [49]. The parameters used in these simulations were a beam spot 6 mm in diameter (defined by the actual size of the Li target) and a 2.3 keV energy spread of the proton beam (the nominal 0.1% energy stability of the accelerator).

The corresponding neutron spectra are plotted in Fig. 3. Before the activations the Van de Graaff accelerator was switched to pulsed mode (1 MHz repetition rate, 10-ns pulse width) for calibration of the proton- energy scale by scanning over the 1881 keV threshold of the $^7\text{Li}(p,n)$ reaction. The actual activations were then carried out with the accelerator operated in DC mode. In the close geometry between Li target and samples the mean neutron exposure of the samples was about 1×10^9 and 8×10^9 s⁻¹ during the irradiations at 25 and 473 keV, respectively.

Throughout the activations the relative neutron flux was recorded in intervals of 90 s using a ⁶Li-glass detector at about 1 m from the target. This information was required for later correction of the number of nuclei, which decayed during the irradiation (Sec. III A). The parameters of the three activations are summarized in Table I. Because of the comparably short

half-life of 198 Au ($t_{1/2} = 2.70$ days), the gold reference foils have been changed every 5–6 days.

3. Activations with thermal neutrons at ATI Vienna

The activations with thermal neutrons (kT = 25 meV; 300 K) were performed at the TRIGA Mark-II reactor in a well-characterized thermal spectrum. The neutron flux at the irradiation position about 1 m from the core was $3.9 \pm 0.2 \times 10^{11}$ cm⁻²s⁻¹. This position provides a thermal to epithermal flux ratio of 76 (verified via the Zr standard method; for details, see Ref. [50]).

In total, two irradiations of 570 and 3595 s were performed. The neutron fluence was determined by means of Zr foils attached to the vials via the induced 95 Zr activity, using the thermal cross section value for 94 Zr(n, γ) of (49.4 \pm 1.7) mb [26]. The activities of these foils indicated flux variations of up to 5% between different activations reflecting small variations in the reactor power between these activations.

B. AMS measurements

As shown in the sketch of the VERA facility in Fig. 4, negative molecular ions (BeO⁻) extracted from a cesium sputter source are selected in a low-energy mass spectrometer consisting of an electrostatic analyzer and a double-focussing dipole magnet before they are injected into the tandem accelerator,

TABLE III. Systematic uncertainties of the neutron fluence for KIT activations.

Source of uncertainty	Uncertainty (%)
Neutron fluence	
 Gold cross section 	$1.8/1.0^{a}$
— Mass of gold samples	0.3
$-\gamma$ efficiency	2.0
$-\gamma$ intensity per decay	0.12
— Time factors	< 0.1
 Gold counts and background 	<1.5
Total	3.1/2.7

^aFor neutron energies of 25 (q-MB) and 473 keV, respectively.

alternating between ${}^9\mathrm{Be^{16}O^-}$ and ${}^{10}\mathrm{Be^{16}O^-}$, respectively. In the terminal of the tandem a gas stripper is producing positive ions for the second acceleration stage and destroys any molecular ions including molecular isobars. Depending on the method used for ${}^{10}\mathrm{Be}$ counting in a specific particle detector, a particular charge state (either 2^+ or 3^+) is selected after the accelerator, in a second (high-energy) mass spectrometer. The isotope ratio ${}^{10}\mathrm{Be}/{}^9\mathrm{Be}$ is eventually obtained by a current measurement of the stable ${}^9\mathrm{Be}$ ions in a Faraday cup followed by a count-rate measurement of the rare isotope ${}^{10}\mathrm{Be}$ in the energy detectors, either the Gas-absorber–E-detector (method a) [33,46,51] or the $\Delta\mathrm{E}$ -E detector (method b) in combination with a degrader foil for ${}^{10}\mathrm{B}$ separation [44,45].

Since isobaric interferences are a major challenge in the AMS measurements of irradiated samples of such low isotopic ratios, extensive background studies were performed prior to the irradiations in order to demonstrate that the required sensitivity can be achieved. Two different setups were used at VERA for the 10 Be measurements: (a) "setup a" (gas absorber method), consisting of a thick "absorber" (foil and gas volume) in front of a particle detector that stops essentially all isobaric 10 B ions before entering the final detector. Using this setup a machine background of 10 Be/ 9 Be $\sim 10^{-14}$ at/at was achieved. In these cases, where signal and background will be of the same order as in the present work (see Sec. II A), a constant and well-defined background signal is mandatory. This goal was achieved for "setup a" with a measurement reproducibility of about 1%.

TABLE IV. Gold reference cross sections and neutron fluence data.

Sample	E_p (keV)	Gold cross section ^a (mb)	Neutron fluence Φ_{tot} (10 ¹⁵ cm ⁻²)
	(q-MB ^b at $kT = 25 keV$	
BeO-1	1912	640 ± 11	1.16 ± 0.04
BeO-2	1912	640 ± 11	1.91 ± 0.06
		$\overline{E}_n = 473 \pm 53 \text{ keV}$	
BeO-3	2284	142.7 ± 1.4	3.31 ± 0.10

^aSpectrum averaged values.

TABLE V. Systematic uncertainties of the neutron fluence for the thermal activations.

Source of uncertainty	Uncertainty (%)
Neutron fluence	
— Zr cross section	3.4
 Epithermal correction & geometry 	3
— Mass of Zr samples	0.3
— γ efficiency	2.0
 γ intensity per decay 	0.5
— Time factors	< 0.1
 Zr counts and background 	<1.5
Total	5.0

The second "setup b" used in this work utilized the "degrader foil method," where a thick foil that is traversed by the particle beam causes a difference in the residual energy of the transmitted isobars 10 B and 10 Be. These ions could be spatially separated in a subsequent magnetic analysis which resulted in a complete 10 B suppression. With this setup the background level for 10 Be/ 9 Be was found to be well below 10^{-15} at/at. A reproducibility for 10 Be/ 9 Be for samples made from identical reference material (and not limited by counting statistics) of $\sim 3\%$ was observed with this method at VERA. The detector for "setup b" is based on a compact type of gas ionization chamber [52,53], which offers a significantly improved energy resolution and is, therefore, ideally suited for particle energies typical at VERA.

Both detectors had been proven to provide sufficient suppression of remaining ¹⁰B ions in the beam [47]. Isobaric interferences from ¹⁰B could easily be discriminated [33,44,45,47] and had no impact on the final AMS results.

The ¹⁰Be/⁹Be isotope ratios in non-irradiated blanks were quantified in a series of test measurements, resulting in the isotope ratios listed as "intrinsic ¹⁰Be content" in Tables I and II. As the signal expected from the neutron irradiations is similar compared to the ¹⁰Be content of the nonirradiated material, the background stability of the VERA setup [54,55] was crucial for the experiment and has been verified by detailed test runs. The uncertainty contribution from the intrinsic ¹⁰Be content in the non-irradiated sample and from measurement background contributed between 3% (25 keV samples) and 6% (473 keV sample) to the final uncertainty. This background contribution, however, was negligible for the samples irradiated with thermal neutrons due to their 100 times higher isotope ratios compared to the "keV samples."

III. DATA ANALYSIS AND RESULTS

A. Determination of neutron fluence

The induced activities of the Au flux monitor foils were measured using high-purity germanium (HPGe) detectors selecting a distance of 76 ± 1 mm to the Au foils. The γ efficiency was determined with a set of accurate reference sources and was known with an uncertainty of $\pm2.0\%$. The corrections due to coincidence summing and sample extension were minimized by keeping the distance between sample and detector much larger than the respective diameters.

^bQuasi-Maxwell-Boltzmann distribution simulating a thermal spectrum at kT = 25 keV.

TABLE VI. Uncertainty contribution from the AMS measurements.

Source of uncertainty		Uncertainty (%)	
	25 keV	473 keV	Thermal
¹⁰ Be standard	3	3	3
Atom counting statistics	2	8	1
AMS reproducibility	2	3	2
¹⁰ Be blank	3	6	_
Total	5.1	11	3.7

The number of counts C in the characteristic 411.8 keV line in the γ -ray spectrum recorded during the measuring time t_m is related to the number of produced nuclei N_{198} at the end of irradiation by

$$N_{198} = \frac{C}{K_{\gamma} \epsilon_{\gamma} I_{\gamma} (1 - e^{-\lambda t_m}) e^{-\lambda t_w}},\tag{1}$$

where ϵ_{γ} denotes the detector γ -ray detection efficiency and t_w the waiting time between irradiation and activity measurement. The decay rate $\lambda = 0.25718(7)d^{-1}$ and the intensity per decay, $I_{\gamma} = 95.58(12)\%$ of ¹⁹⁸Au were adopted from Ref. [56]. The factor K_{γ} describes the γ -ray self absorption in the sample, which is for the thin gold samples used in this work in very good approximation [57]:

$$K_{\gamma} = \frac{1 - e^{-\mu x}}{\mu x}.\tag{2}$$

The γ -ray absorption coefficient μ were taken from Ref. [58]. The gold samples were x=20–30 μ m in thickness, yielding self-absorption corrections $K_{\gamma}=0.996$ –0.994. Accordingly, the associated uncertainties had no effect on the overall uncertainty budget and were neglected.

The number of produced nuclei N_{198} can also be expressed by the neutron fluence $\Phi_{\rm tot} = \int_0^{t_a} \Phi(t) dt$, the corresponding spectrum-averaged capture cross section $\langle \sigma \rangle$, the decay correction f_b , and the number of irradiated atoms in the sample

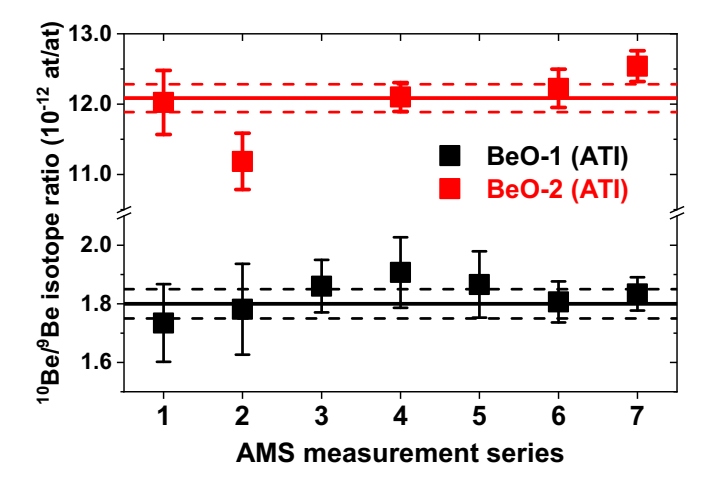


FIG. 5. ¹⁰Be/⁹Be ratios for the two samples irradiated with thermal neutrons from a TRIGA reactor. The solid and dashed lines represent the weighted mean and the standard deviation of the mean.

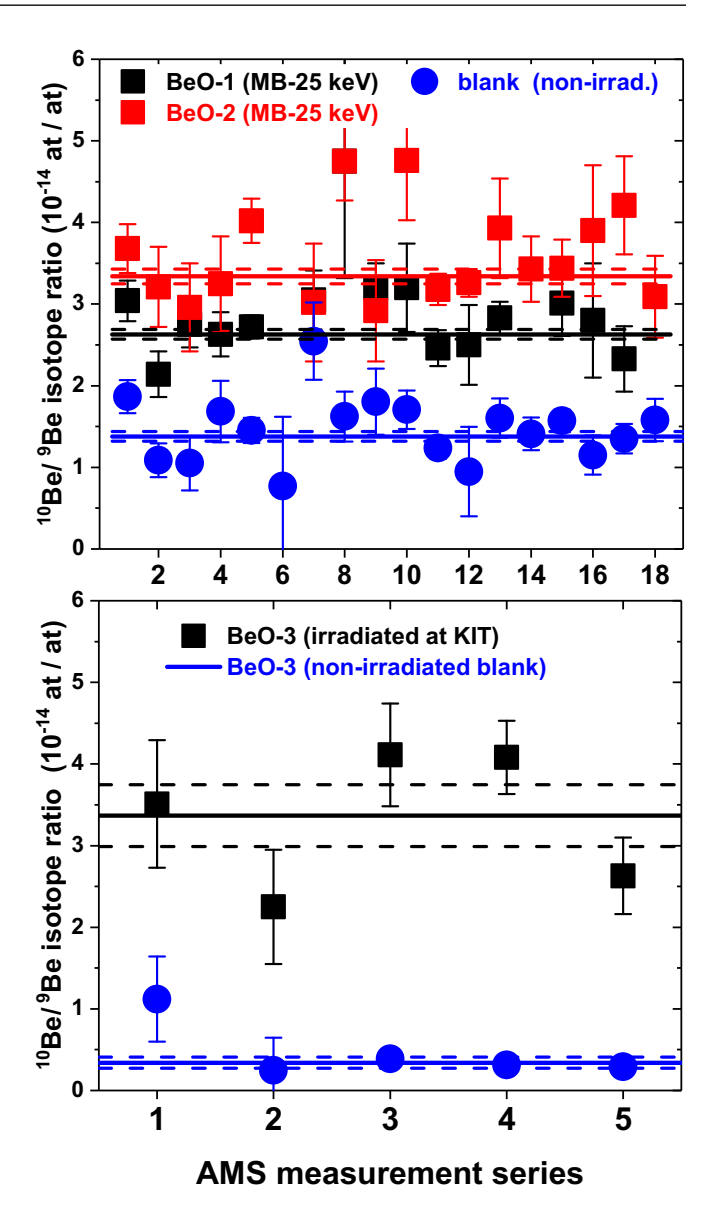


FIG. 6. 10 Be/ 9 Be ratios for the two samples irradiated with a quasistellar Maxwell-Boltzmann spectrum (MB-25 keV) as obtained during the various AMS beam times (upper panel). The lower panel gives the results for the sample irradiated with 473 \pm 53 keV (BeO-3). The solid and dashed lines represent the weighted mean and the standard deviation of the mean.

 N_{197} as

$$N_{198} = \Phi_{\text{tot}} N_{197} \langle \sigma \rangle f_b. \tag{3}$$

The factor f_b , which corrects for the fraction of activated nuclei that decay already during irradiation, is

$$f_b = \frac{\int_0^{t_a} \Phi(t) e^{-\lambda(t_a - t)} dt}{\int_0^{t_a} \Phi(t) dt},$$
 (4)

where $\Phi(t)$ denotes the neutron fluence rate during the irradiation and λ the decay rate of the product nucleus ¹⁹⁸Au.

For the gold reference cross section in the energy range of the 25 keV quasi-MB spectrum we used the new

TABLE VII. Results from the activations at thermal neutron energies.

Sample	Neutron fluence ^a (10 ¹⁴ cm ⁻²)	10 Be/ 9 Be (10 ⁻¹² at/at)	Thermal cross section (mb)
BeO-ATI1	2.22 ± 0.11	1.80 ± 0.07	8.11 ± 0.54
BeO-ATI2	14.02 ± 0.70	11.93 ± 0.45	8.51 ± 0.57
Mean			8.31 ± 0.52

^aThermal equivalent neutron fluence (ATI values include 7% correction for epithermal contribution of Zr monitor foils).

standard value for kT = 30 keV. An evaluation of neutron standards was recently published giving a cross-section value for 197 Au (n, γ) of (620 ± 11) mb, which was defined as a standard for kT = 30 keV [59,60]. This standard value was normalized to the experimental neutron spectrum resulting in a spectrum-averaged gold cross-section value for the 25 keV quasi-Maxwellian spectrum of 640 ± 11 mb. This value is within 1% of the prescription of the new version KADoNiS v1.0 (Karlsruhe Astrophysical Database of Nucleosynthesis in Stars) [61], which itself is based on the weighted average of recent data from measurements at GELINA [62] and n_TOF [63,64], and in agreement with a recent activation measurement [65]. Note, the effective values listed in column three of Table IV are reflecting a change of 5.8% in the gold reference cross section compared to the values previously used in similar activation experiments.

For the 473 ± 53 keV spectrum, where the (n, γ) cross section of gold is an established standard [60,66], the evaluated data from the ENDF/B-VII.1 library have been used. The respective spectrum-averaged gold cross sections are listed in Table IV.

The main contributions to the total uncertainty of the neutron fluence for the keV activations are due to the γ efficiency of the HPGe detector and to the Au reference cross sections (Table III).

In the short activations at ATI decay correction was negligible because the half-life of the activation product 95 Zr was much longer than the irradiation times. In the ATI activations, the total production of 95 Zr consists of the thermal part ($\sigma_{th} = 49.4 \pm 1.7$ mb) and the epithermal part (the resonance integral RI = 280 ± 10 mb) [26,27] with the epithermal flux being 1/76 of the thermal flux for this irradiation setup [50].

TABLE IX. Adopted resonance parameters [26].

Resonance energy (keV)	J	ℓ	Γ (keV)	$2g\Gamma_n$ (keV)	Γ_{γ} (eV)
$622.0 \pm 0.8 \\ 811.8 \pm 0.7$	-	2	17.5 ± 0.5 7.0 ± 0.9	30.63 ± 0.88 8.75 ± 1.20	0.73 ± 0.10 0.73^{a}

^aNot, known; the same value was assumed as for 622.0 keV.

Therefore, an additional 7% of the total ⁹⁵Zr production was due to the epithermal neutrons. This contribution was corrected for in the calculation of the thermal neutron fluence (Table VII).

For ${}^9\mathrm{Be}(n,\gamma){}^{10}\mathrm{Be}$, the ratio of the epithermal to the thermal cross section is much lower, with $\sigma_{th}=8.49\pm0.34$ mb and RI = 3.8 ± 0.2 mb [26,27], about $1/10^{th}$ of the ${}^{94}\mathrm{Zr}$ case. The equivalent correction for the ATI activation for ${}^9\mathrm{Be}(n,\gamma){}^{10}\mathrm{Be}$ was therefore <1%. The final accuracy of the neutron fluence for the ATI setup was dominated by the uncertainty of the ${}^{94}\mathrm{Zr}(n,\gamma){}^{95}\mathrm{Zr}$ cross section (3.4%), the epithermal correction and reproducibility of the irradiation geometry (3%) and the γ efficiency of the Ge detector (2%). In the end the fluence for the ATI samples could be determined with an uncertainty of about 5% (see Table V).

B. AMS results and spectrum averaged cross sections

Because inherent effects such as mass fractionation, machine instabilities, or potential beam losses between the current measurement and the respective particle detector are difficult to quantify in an absolute way to better than 5 to 10%, accurate AMS measurements depend on well-defined reference materials. Therefore, the isotope ratios 10 Be/ 9 Be have been measured relative to a 10 Be/ 9 Be standard.

The background-corrected and normalised ${}^{10}\mathrm{Be}/{}^{9}\mathrm{Be}$ isotope ratios are determined via

$$\frac{^{10}\text{Be}}{^{9}\text{Be}}\Big|_{\text{act}} = \left[\frac{^{10}\text{Be}}{^{9}\text{Be}}\Big|_{\text{sample}} - \frac{^{10}\text{Be}}{^{9}\text{Be}}\Big|_{\text{blank}}\right] * f_{\text{norm}}, \quad (5)$$

where f_{norm} denotes the normalization factor obtained via the available ¹⁰Be standard that was known with an uncertainty of 3%.

All AMS data obtained in this work were normalised to the 10 Be-standard S555N with a nominal value of 10 Be 9 Be =

TABLE VIII. Measured spectrum averaged cross sections.

E_n (keV)	Sample	¹⁰ Be/ ⁹ Be r	10 Be/ 9 Be ratio (10 $^{-14}$ at/at)		Cross section (μb)	
		Measured	Blank-subtracted			
25 (q-MB)	BeO-1 ^a	2.62 ± 0.08	1.24 ± 0.08		10.71 ± 0.79	
	BeO-2 ^a	3.34 ± 0.13	1.96 ± 0.11		10.32 ± 0.64	
	Blank BeO ^a	1.38 ± 0.06				
				Mean value	10.44 ± 0.63	
473±53	BeO-3 ^b Blank BeO ^b	3.18 ± 0.35 0.41 ± 0.13	2.77 ± 0.31		8.4 ± 1.0	

^aBeO, commercial from Alfa Aesar.

^bBeO, extracted from the mineral Phenakite.

TABLE X. Measured cross sections from this work compared to spectrum averaged values from evaluated data (all values in μ b).

Neutron energy	Eva	Evaluated cross sections (μ b)				
(keV)	ENDF/B-VII.1 [20]	JENDL-4.0 [21]	JEFF-3.3 [22]	Measured	Best fit	
25 ^a	9.7	7.9	11.8	10.4 ± 0.6	10.2	
473 ± 53	3.1	2.0	11.6	8.4 ± 1.0	8.1	

^aQuasi-Maxwellian spectrum.

 $(8.71 \pm 0.24) \times 10^{-11}$ at/at [67] The final uncertainties of the mean isotope ratios are determined by a 3% contribution from the ¹⁰Be standard, 3% (1%) from the reproducibility in the ¹⁰Be measurements using detector "setup b" ("setup a"), the uncertainty of the intrinsic ¹⁰Be content in the samples BeO-1 and BeO-2 (3%) and BeO-3 (6%), and by statistical uncertainties of 2 and 8% for the values at 25 and 473 keV, respectively (see Table VI).

The ¹⁰Be/⁹Be ratios of the two samples irradiated at ATI with thermal neutrons, as measured in various AMS beam times are plotted in Fig. 5. The solid and dashed lines represent the weighted mean and the standard deviation of the mean for the respective samples.

The ¹⁰Be/⁹Be ratios of the samples BeO-1 and BeO-2 irradiated at KIT, as measured during 15 and 17 AMS beam times, respectively, are plotted in the upper panel of Fig. 6 together with the corresponding ratios of the blank samples. The solid and dashed lines represent the weighted mean and the standard deviation of the mean for the respective samples. Similarly, the lower panel in Fig. 6 gives the AMS data for the sample BeO-3 (473 keV mean neutron energy) and the corresponding blank sample.

The spectrum-averaged ${}^{9}\text{Be}(n, \gamma)$ cross section can directly be calculated from the measured isotope ratios and the

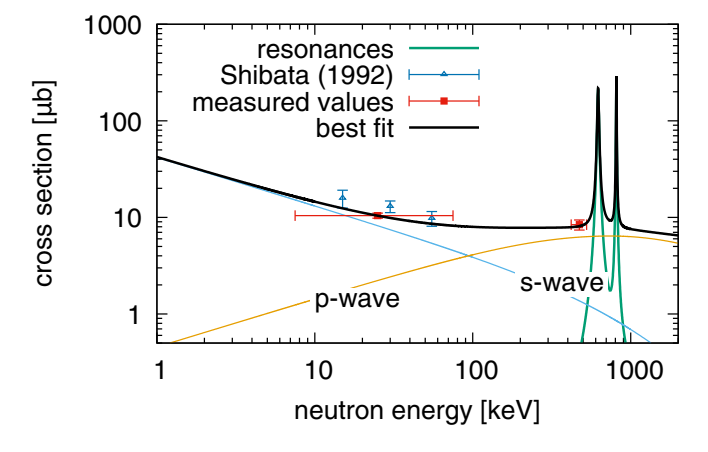


FIG. 7. The horizontal error bars for the measured data points represent the width of the neutron energy distribution at 25 and 473 keV, respectively. The best fit (solid line) to the experimental data (squares) is essentially determined by direct radiative capture, i.e., by the sum of s- and p-wave components (thin solid lines). The contributions from higher lying resonances at 622 and 811.8 keV [26] are indicated by a solid line. Within uncertainties, previous unpublished data from TIT [25] and the present fit are well compatible.

total neutron fluence Φ_{tot} ,

$$\sigma_{\rm exp} = \frac{1}{\Phi_{\rm tot}} \times \frac{^{10}{\rm Be}}{^{9}{\rm Be}} \bigg|_{\rm act}, \tag{6}$$

completely independent of the sample mass and the decay properties of the product nucleus. The resulting cross-section values are summarized in Tables VII and VIII. These data supersede the preliminary results reported earlier [33,51].

IV. MAXWELLIAN AVERAGE CROSS SECTIONS (MACS)

In the astrophysically relevant energy range below a few hundred keV the (n, γ) cross section of ⁹Be is dominated by the direct radiative capture (DRC) mechanism, because the first resonances, located at 622 and 811.8 keV [26], are $\ell > 0$ resonances and there are no $J = 1^-$ or 2^- in 10 Be (which can be formed by s-wave neutrons) with a 1/v resonance tail in the low-energy side. The DRC interactions by s-wave neutrons are characterized by a 1/v-component that can be normalized via the accurate thermal cross section of 8.31 ± 0.52 mb (measured in this work), yielding a contribution of $8.5 \mu b$ at 25 keV neutron energy. The additional p-wave component, which is linearly increasing with neutron velocity, is due mostly to capture into the $J = 1^-$ state at 5.96 MeV and, to a minor extent, to the $J = 2^-$ state at 6.26 MeV in ¹⁰Be.

The p-wave component of the capture cross section has been calculated using the DRC model described in Ref. [68], using experimental information on the bound states to calculate the wave functions and matrix elements for electric dipole

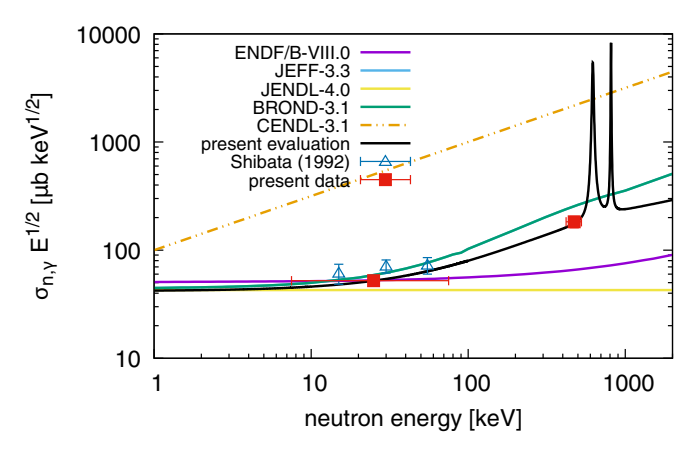


FIG. 8. Comparison of experimental data in the neutron energy range of interest for s process nucleosynthesis calculations with evaluated (n, γ) cross sections of ⁹Be as given in the main data libraries. The data are plotted as reduced cross sections, i.e., the cross section is multiplied by \sqrt{E} .

kT (keV)	ENDF/B-VII.1	JENDL-4.0	JEFF-3.3	KADoNiS-v1.0	This work			
	[20]	[21]	[22]	[9]	DRC-s	DRC-p	Resonances	Total MACS
5	21.9	18.1	20.9	18.2 ± 5.5	17.6	1.6	<0.1	19.2 ± 0.9
10	15.6	12.8	16.3	14.2	12.4	2.2	< 0.1	14.6 ± 0.7
15	12.9	10.5	14.5	12.6	10.0	2.6	< 0.1	12.6 ± 0.6
20	11.2	9.07	13.7	11.9	8.6	3.0	< 0.1	11.6 ± 0.6
25	10.1	8.11	13.2	11.4	7.7	3.4	< 0.1	11.1 ± 0.6
30	9.31	7.41	12.9	11.1 ± 1.6	7.0	3.6	< 0.1	10.6 ± 0.5
40	8.17	6.42	12.6	10.9	6.0	4.1	< 0.1	10.1 ± 0.6
50	7.39	5.74	12.4	10.8	5.3	4.4	< 0.1	9.7 ± 0.6
60	6.82	5.24	12.0	10.8	4.5	4.7	< 0.1	9.3 ± 0.6
80	6.02	4.54	12.5	10.8	4.0	5.2	0.5	9.7 ± 0.7
100	5.48	4.06	12.6	10.9 ± 3.3	3.5	5.5	1.2	10.2 ± 0.8

TABLE XI. Maxwellian averaged cross sections (μ b).

transitions. The DRC p-wave component contributes with 2.2 and 6.2 μ b at 25 and 473 keV incident neutron energies, respectively. Accordingly, this component contributes about 30% of the 25 keV MACS and starts to dominate the cross section with increasing energies, in contrast to the cross-section shape assumed for the evaluations in the ENDF/B-VII.1 and JENDL-4.0 libraries (Fig. 1).

The additional small cross-section component due to the resonances at 622 and 811.8 keV has been considered by an R-matrix calculation using the SAMMY code [69] with the resonance parameters adopted from Ref. [26] (Table IX). This part was found negligible for the quasi-stellar spectrum at 25 keV (0.03%) but contributes 8.5% to the value at 473 keV.

The sum of the two DRC components and the resonant cross section exceeded the measured cross sections at 25 and at 473 keV. While the s-wave DRC component was fixed by the thermal cross section the p-wave part could be tuned within the uncertainty of the calculation. It turned out that the experimental data points could be reproduced well within uncertainties (Table X) by a 30% reduction of the p-wave DRC contribution. The so obtained best-fit solution for the

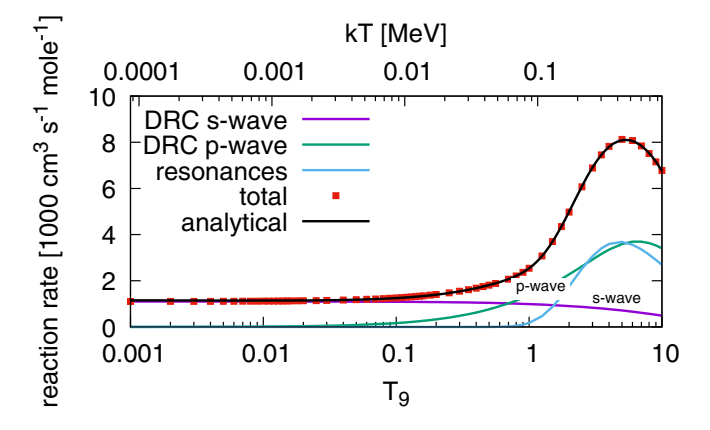


FIG. 9. Reaction rate for the ${}^9\mathrm{Be}(\mathsf{n},\gamma)$ reaction in the thermal range of interest for s process nucleosynthesis calculations. T_9 is the temperature in units of 10^9 Kelvin. The analytical expression which accurately reproduces the tabulated cross sections (see Table XI) is given in the text.

energy-dependent cross section is compared in Fig. 7 with the experimental results.

The best fit obtained with the present results shows fair agreement with a previous measurement at TIT, which yielded spectrum-averaged cross sections of 15.8 ± 4.7 , 10 ± 3.1 , and $9.8 \pm 2.9 \ \mu b$ at 15, 30, and 55 keV, respectively [25].

Using the best-fit solution for the energy-dependent cross section (Fig. 7), MACS values were calculated for thermal energies between kT=5 to 100 keV. The *s*-wave DRC component, which dominates the energy region below 25 keV, is determined with an uncertainty of 4% via normalization of the thermal cross section. The *p*-wave DRC component, which becomes increasingly important at higher thermal eneries, is adjusted to match the measured data points at 25 and 473 keV, and carries, therefore, an uncertainty of 10%. The resonant part of the cross section contributes only at very high temperatures, i.e., for kT values above 60 keV, with estimated uncertainties of 20% corresponding to the resonance parameters in Table IX [26].

Accordingly, the MACS uncertainties listed in Table XI were determined by weighting the uncertainties of each component according to their contribution to the respective total MACS value.

The comparison of the MACS data of Table XI confirms that the data sets in the ENDF/B-VII.1 [20] and JENDL-4.0 [21] libraries are only adequate at neutron energies below about 10 keV because of the neglected p-wave DRC component. The JEFF-3.3 evaluation exhibits fair agreement as far as the energy dependence is concerned but yields MACS values that are too high by 8, 20, and 25% at kT = 5, 20, and 100 keV, respectively. Within uncertainties, the values of the KADoNiS compilation [9], which considered already the preliminary results of this work [33,51], are consistent with the present data. However, the overall uncertainties could be reduced by factors of 3 to 5.

From the total capture cross section, consisting of DRC *s*-and *p*-wave plus the resonance components, the Maxwellian averaged at various thermal energies can be readily calculated and from that, a reaction rate,

$$N_A \langle \sigma v \rangle = a_0 \left(1 + a_1 T_9^{1/2} + a_2 T_9 + a_3 T_9^{3/2} + a_4 T_9^2 + a_5 T_9^{5/2} \right) + a_6 T_9^{-3/2} e^{-b_0/T_9}, \tag{7}$$

in units of cm³/s/mole when $a_0 = 1166.2$, $a_1 = -0.420$, $a_2 = 2.362$, $a_3 = -1.044$, $a_4 = 0.168$, $a_5 = -0.011$, $a_6 = 1.706 \times 10^5$, and $b_0 = 7.087$, can be derived. Here, T_9 is the temperature in units of 10^9 Kelvin.

V. SUMMARY

Neutron activations at the Karlsruhe Van de Graaff accelerator and a TRIGA reactor have been combined with single-atom counting by accelerator mass spectrometry at the Vienna Environmental Research Accelerator VERA. Sensitive measurements of the ${}^9\mathrm{Be}(n,\gamma){}^{10}\mathrm{Be}$ cross section were performed in a quasistellar spectrum corresponding to a thermal energy of $kT=25~\mathrm{keV}$ and at higher energies using a spectrum centered at $473\pm53~\mathrm{keV}$. With the resulting cross sections of 10.4 ± 0.6 and $8.4\pm1.0~\mu\mathrm{b}$ it was possible to constrain the s- and p-wave DRC components for a consistent descrip-

tion of the cross section as a function of neutron energy. At higher energies the contributions from resonances at 622 and 812 keV were considered as well. From these data Maxwellian average cross sections could be calculated for thermal energies between kT = 5 and 100 keV with uncertainties of 6 to 10%. Compared to existing data the uncertainties could be reduced by factors of three to five. We also report a new measurement of the thermal cross-section for ${}^{9}\text{Be}(n, \gamma){}^{10}\text{Be}$ of 8.31 ± 0.52 mb.

ACKNOWLEDGMENTS

This work was partly funded by the Austrian Science Fund (FWF), Projects No. P20434 and No. I428, and by the Australian Research Council, Projects No. DP140100136 and No. DP180100496. We thank Peter Kubik (ETH Zurich, Switzerland) for generously providing the ¹⁰Be/⁹Be standard material for the AMS measurement.

- [1] E. Burbidge, G. Burbidge, W. Fowler, and F. Hoyle, Rev. Mod. Phys. 29, 547 (1957).
- [2] A. Cameron, Technical report, A. E. C. L. Chalk River, Canada, 1957 (unpublished).
- [3] R. Gallino et al., Ap. J. 497, 388 (1998).
- [4] A. Karakas and J. Lattanzio, Publ. Astron. Soc. Australia 31, e030 (2014).
- [5] S. Bisterzo *et al.*, Mon. Not. Royal Astron. Soc. **449**, 506 (2015).
- [6] C. Raiteri et al., Ap. J. 419, 207 (1993).
- [7] L. The, M. El Eid, and B. Meyer, Ap. J. 655, 1058 (2007).
- [8] M. Pignatari et al., Ap. J. 762, 31 (2013).
- [9] I. Dillmann et al., in Nuclei in the Cosmos XIII, PoS— Proceedings of Science, edited by Z. Fülöp (SISSA, Trieste, 2014), contribution 057, http://pos.sissa.it.
- [10] D. Kasen, B. Metzger, J. Barnes, E. Quataert, and E. Ramirez-Ruiz, Nature 551, 80 (2017).
- [11] A. Wallner et al., Nat. Commun. 6, 5956 (2015).
- [12] Y.-Z. Qian and G. Wasserburg, Phys. Rep. 442, 237 (2007).
- [13] F.-K. Thielemann *et al.*, Prog. Particle Nucl. Phys. **66**, 346 (2011).
- [14] T. Rauscher, AIP Advances 4, 041012 (2014).
- [15] S. Woosley and T. Janka, Nat. Phys. 1, 147 (2005).
- [16] A. Arcones and F.-K. Thielemann, J. Phys. G 40, 013201 (2013).
- [17] K. Farouqi et al., Ap. J. 712, 1359 (2010).
- [18] A. Bartlett, J. Gorres, G. J. Mathews, K. Otsuki, M. Wiescher, D. Frekers, A. Mengoni, and J. Tostevin, Phys. Rev. C. 74, 015802 (2006).
- [19] J. Görres, H. Herndl, I. J. Thompson, and M. Wiescher, Phys. Rev. C. 52, 2231 (1995).
- [20] M. Chadwick et al., Nucl. Data Sheets 112, 2887 (2011).
- [21] K. Shibata et al., J. Nucl. Sci. Tech. 48, 1 (2011).
- [22] Technical report, OECD Nuclear Energy Agency, Paris, (unpublished), https://www.oecd-nea.org/dbdata/jeff/jeff33/.
- [23] A. I. Blokhin, E. V. Gai, A. V. Ignatyuk, I. I. Koba, V. N. Manokhin, and V. N. Pronyaev, Technical Report Yad. Reak. Konst. No. 2, p. 62 (2016).

- [24] Z. G. Ge et al., J. Kor. Phys. Soc. **59**, 1052 (2011).
- [25] S. Shibata, Master Thesis, 1992, in Japanese (unpublished).
- [26] S. Mughabghab, in *Atlas of Neutron Resonances*, 5th ed. (Elsevier, Amsterdam, 2006).
- [27] B. Pritychenkov and S. Mughabghab, Nucl. Data Sheets 113, 3120 (2012).
- [28] R. B. Firestone and Z. Révay, Phys. Rev. C. 93, 054306 (2016).
- [29] G. Korschinek et al., Nucl. Instr. Meth. B 268, 187 (2010).
- [30] J. Chmeleff et al., Nucl. Instr. Meth. B 268, 192 (2010).
- [31] H.-A. Synal, Int. J. Mass Spectrom. **349-350**, 192 (2013).
- [32] W. Kutschera, Int. J. Mass Spectrom. **349-350**, 203 (2013).
- [33] A. Wallner, Nucl. Instr. Meth B 268, 1277 (2010).
- [34] P. Steier et al., Nucl. Instr. Meth. B 240, 445 (2005).
- [35] H. Nassar, M. Paul, I. Ahmad, D. Berkovits, M. Bettan, P. Collon, S. Dababneh, S. Ghelberg, J. P. Greene, A. Heger, M. Heil, D. J. Henderson, C. L. Jiang, F. Käppeler, H. Koivisto, S. OBrien, R. C. Pardo, N. Patronis, T. Pennington, R. Plag, K. E. Rehm, R. Reifarth, R. Scott, S. Sinha, X. Tang, and R. Vondrasek, Phys. Rev. Lett. 94, 092504 (2005).
- [36] G. Rugel et al., Nucl. Inst. Meth. B 259, 683 (2007).
- [37] I. Dillmann, C. Domingo-Pardo, M. Heil, F. Käppeler, A. Wallner, O. Forstner, R. Golser, W. Kutschera, A. Priller, P. Steier, A. Mengoni, R. Gallino, M. Paul, and C. Vockenhuber, Phys. Rev. C. 79, 065805 (2009).
- [38] I. Dillmann et al., Nucl. Instr. Meth. B 268, 1283 (2010).
- [39] A. Wallner et al., Phys. Rev. Lett. 112, 192501 (2014).
- [40] A. Wallner, M. Bichler, K. Buczak, I. Dillmann, F. Käppeler, A. Karakas, C. Lederer, M. Lugaro, K. Mair, A. Mengoni, G. Schätzel, P. Steier, and H. P. Trautvetter, Phys. Rev. C. 93, 045803 (2016).
- [41] P. Ludwig, G. Rugel, I. Dillmann, T. Faestermann, L. Fimiani, K. Hain, G. Korschinek, J. Lachner, M. Poutivtsev, K. Knie, M. Heil, F. Käppeler, and A. Wallner, Phys. Rev. C. 95, 035803 (2017).
- [42] A. Wallner, K. Buczak, T. Belgya, M. Bichler, L. Coquard, I. Dillmann, R. Golser, F. Käppeler, A. Karakas, W. Kutschera, C. Lederer, A. Mengoni, M. Pignatari, A. Priller, R. Reifarth, P. Steier, and L. Szentmiklosi, Phys. Rev. C. 96, 025808 (2017).

- [43] W. Ratynski and F. Käppeler, Phys. Rev. C 37, 595 (1988).
- [44] O. Forstner et al., Nucl. Instr. Meth. Phys. Res. B 266, 2213 (2008).
- [45] M. Martschini, Master thesis at the University of Vienna, 2008 (unpublished).
- [46] A. Priller et al., Nucl. Instr. Meth. Phys. Res. B 223-224, 601 (2004).
- [47] P. Steier et al. (unpublished).
- [48] S. Merchel *et al.*, Nucl. Instr. Meth. Phys. Res. B 266, 4921 (2008).
- [49] R. Reifarth, M. Heil, F. Käppeler, and R. Plag, Nucl. Instr. Meth. A 608, 139 (2009).
- [50] C. Vockenhuber, M. Bichler, A. Wallner, W. Kutschera, I. Dillmann, and F. Käppeler, Phys. Rev. C 77, 044608 (2008).
- [51] A. Wallner et al., J. Phys. G: Nucl. Part. Phys. 35, 014018 (2008).
- [52] M. Döbeli et al., Nucl. Instr. Meth B 219-220, 415 (2004).
- [53] M. Suter et al., Nucl. Instr. Meth B 259, 165 (2007).
- [54] A. Wallner et al., Eur. J. Phys A. 27, 337 (2006).
- [55] A. Wallner et al., Nucl. Instr. Meth. B 259, 677 (2007).
- [56] Z. Chunmei, Nucl. Data Sheets 95, 59 (2002).
- [57] W. Dixon, Nucleonics 8, 68 (1951).
- [58] NIST, Technical report, National Institute of Standards and Technology, http://www.nist.gov/pml/data/xraycoef/index.cfm (unpublished).

- [59] A. Carlson et al., Nucl. Data Sheets 148, 143 (2018).
- [60] A. Carlson et al., Nucl. Data Sheets 118, 126 (2014).
- [61] I. Dillmann et al., Nucl. Data Sheets 120, 171 (2014).
- [62] C. Massimi et al., Eur. Phys. J. A 50, 124 (2014).
- [63] C. Massimi et al. (n_TOF collaboration), Phys. Rev. C 81, 044616 (2010).
- [64] C. Lederer et al., Phys. Rev. C 83, 034608 (2011).
- [65] P. Jiménez-Bonilla and J. Praena, in *Nuclei in the Cosmos XIII*, PoS—Proceedings of Science, edited by Z. Fülöp (SISSA, Trieste, 2015), contribution 102, http://pos.sissa.it.
- [66] A. Carlson et al., Kor. J. Nucl. Sci. Tech. **59**, 1390 (2011).
- [67] P. Kubik, M. Christl, and V. Alfimov, New primary ¹⁰Be standard and t_{1/2} for AMS at ETH, Annual Report 2009, p. 12 (https://www.ethz.ch/content/dam/ethz/special-interest/phys/particle-physics/ion-beam-physics-dam/images/LIP_annual_report_2009.pdf).
- [68] A. Mengoni, T. Otsuka, and M. Ishihara, Phys. Rev. C 52, R2334 (1995).
- [69] N. Larson, Technical report, ORNL/TM-9179/R8 and ENDF-364/R2, Oak Ridge National Laboratory, https://info.ornl.gov/ sites/publications/files/Pub13056.pdf.

Correction: The ordinate axis label in Fig. 1 contained an error and has been fixed. Some entries in Tables X and XI needed adjustment and have been resolved.